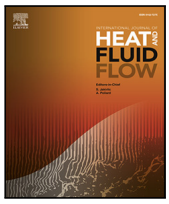
International Journal of Heat and Fluid Flow 120 (2026) 110336



Contents lists available at ScienceDirect

International Journal of Heat and Fluid Flow

journal homepage: www.elsevier.com/locate/ijhff



Work-energy pathway analysis of boundary layer ingestion in propulsive fuselage aircraft

Nicolas G.M. Moirou *, Drewan S. Sanders

Centre for Propulsion and Thermal Power Engineering, Cranfield University, Cranfield, MK43 0AL, Bedfordshire, United Kingdom

ARTICLE INFO

Keywords:
Boundary layer ingestion
Computational Fluid Dynamics
Energy-based analysis
Flow feature segmentation
Propulsion–airframe integration

ABSTRACT

Propulsive fuselage aircraft concepts integrate a rear-mounted propulsion system alongside under-wing turbofans, leveraging fuselage boundary layer ingestion to enhance overall aerodynamic efficiency. Despite its promise, this configuration lacks a universally accepted framework for assessing its aerodynamic benefits, motivating the development of new evaluation methodologies. This study advances a work-energy-based performance accounting framework, formulated in an absolute reference frame, to analyse the aerodynamic mechanisms responsible for energy extraction, deposition, and dissipation within the flow. Aero-propulsive performance is evaluated through flow-feature segmentation, enabling quantitative attribution of energy expenditure to distinct aerodynamic phenomena. The framework is applied to a propulsive fuselage concept, with a parametric exploration of propulsor fan diameter, exhaust configuration, and nozzle geometry. While fan diameter and pressure ratio are primary drivers of performance, exhaust and nozzle shaping exert secondary effects. Notably, improved aft-body performance is achieved through an embedded nacelle trailing edge and a slender, contoured nozzle plug, promoting smoother flow and reduced wake losses, resulting in 2%–5% additional fuel savings. The core contribution lies in the flow-feature segmentation approach, which enables a physically grounded interpretation of complex aerodynamic interactions, provides a robust basis for understanding the impact of design changes, and lays the groundwork for systematic optimisation of integrated propulsion–airframe configurations.

1. Introduction

Propulsive fuselage aircraft are promising concepts for achieving the ambitious environmental targets set by the European Commission (2011). As conventional aircraft approach the limits of achievable improvements in propulsive efficiency (Epstein, 2013), alternative configurations are being explored to harness aerodynamic synergies between the airframe and propulsion system. One such approach involves ingesting the boundary layer (BL) that develops along the fuselage — an idea inspired by marine propulsion systems (Wislicenus, 1960) — to enhance overall aero-propulsive performance.

In conventional tube-and-wing aircraft, podded engines accelerate the free-stream flow to overcome the momentum deficit in the airframe's wake. However, this process imparts excess kinetic energy to both the jet plume and the wake, which is ultimately dissipated as loss. In contrast, boundary layer ingestion (BLI) aircraft act directly on the BL and wake, effectively harvesting their energy, attenuating the wake, and reducing fuel consumption. Amongst the various BLI configurations proposed (Moirou et al., 2023), the propulsive fuselage concept (PFC) stands out for its near-term feasibility due to its compatibility with conventional designs. In this configuration, an aft-mounted propulsor is embedded in the tail cone, enabling effective integration with minimal airframe disruption.

Due to the integrated nature of propulsion and airframe in such concepts, the aerodynamic intricacies render conventional thrust and drag book-keeping schemes (MIDAP Study Group, 1979) inadequate. Traditional methods assume a clear distinction between airframe and propulsion, with drag resulting from viscous–potential flow interactions and thrust serving as a surrogate for useful work. This distinction breaks down in highly integrated designs such as BLI aircraft. Although net aerodynamic forces can still be computed via *near-field* integration, these methods offer limited insight into the underlying physics. Several studies reviewed in Moirou et al. (2023) have proposed alternative momentum-based book-keeping schemes. However, these often mischaracterise thrust as useful work, leading to unphysical results — for instance, apparent propulsive efficiencies exceeding 100%. Furthermore, the causal mechanisms underpinning aerodynamic force generation is often elusive when examined through the lens of momentum balance (Drela, 2021). These limitations have motivated

* Corresponding author.
E-mail address: nicolas.g.moirou@cranfield.ac.uk (N.G.M. Moirou).

https://doi.org/10.1016/j.ijheatfluidflow.2026.110336
Received 17 October 2025; Received in revised form 25 January 2026; Accepted 24 February 2026
Available online 6 March 2026
0142-727X/© 2026 The Authors. Published by Elsevier Inc. This is an open access article under the CC BY license (http://creativecommons.org/licenses/by/4.0/).

Nomenclature

a	Speed of sound, m/s
$C_{\mathcal{X}}$	Coefficient of a power quantity $\mathcal{X}$, $= 2\mathcal{X}/(\rho_\infty V_\infty^3 S_{\text{ref}})$, -
$\dot{\mathcal{E}}$	Mechanical energy flux, J/s
$\dot{\mathcal{E}}_k$	Wake kinetic energy flux, $= \dot{\mathcal{E}}_u + \dot{\mathcal{E}}_v$, J/s
$\dot{\mathcal{E}}_p$	Rate of pressure-defect work, J/s
$\dot{\mathcal{E}}_u$	Stream-wise kinetic energy flux, J/s
$\dot{\mathcal{E}}_v$	Transverse kinetic energy flux, J/s
$\dot{\mathcal{E}}_w$	Lateral wave-outflow energy flux, J/s
$\dot{\mathcal{E}}_\tau$	Rate of viscous boundary work, J/s
$\boldsymbol{\mathcal{F}}$	Force vector on a body, N
$\boldsymbol{f}$	Volume-specific body force vector, N/m^3
f_{plug}	Non-dimensional plug angle, $= \beta_{plug}/\beta_{boat}$, -
H	Total enthalpy, kg m^2/s^{-2}
$\dot{h}$	Rate of change in altitude, m/s
L	Length, m
$\hat{n}$	Unit normal vector, -
$\mathcal{P}_f$	Body force propulsor power, J/s
$\mathcal{P}_K$	Kinetic energy inflow rate, J/s
$\mathcal{P}_S$	Shaft power, J/s
p	Static pressure, Pa
p_G	Gauge static pressure, $= p - p_\infty$, Pa
R, r	Radius, m
$\mathcal{S}$	Control surface, -
$\mathcal{V}$	Control volume, -
$\boldsymbol{V}$	Velocity vector in the absolute reference frame, m/s
$\boldsymbol{V'}$	Velocity vector in the relative reference frame, m/s
W	Aircraft weight, N
$\hat{x}, \hat{y}, \hat{z}$	Cartesian coordinate system in the absolute reference frame, -
$\alpha_{hub}, \alpha_{tip}$	Hub and tip hade angles, °
$\beta_{boat}, \beta_{plug}$	Boat and plug angles, °
$\Delta_{\text{nac,TE}}$	Nacelle trailing edge radial offset coefficient, -
ζ	Shock-wave identifier
Θ	Rate of volumetric pressure work, J/s
μ, μ_t	Laminar and turbulent dynamic viscosities, N s/m^2
ξ	Shear layer identifier
ρ	Density, kg/m^3
$\overline{\overline{\tau}}$	Viscous stress tensor, Pa
Υ	Jet-stream identifier
Φ	Rate of volumetric viscous dissipation, J/s
Φ^*	Total mechanical loss, $= \Phi + \Theta_{\text{irr}}$, J/s

Sub-/Super-scripts

$(\,)_\infty$	Free-stream quantity
$(\,)_{\text{A/C}}$	Aircraft quantity
$(\,)_{\text{B}}$	Body's surfaces' quantity
$(\,)_{\text{fus}}$	Fuselage quantity
$(\,)_{\text{irr, rev}}$	Irreversible and reversible quantities
$(\,)_{\text{MOR}}$	Morphed uninstalled fuselage quantity
$(\,)_{\text{nac}}$	Nacelle quantity
$(\,)_{\text{P}}$	Propulsor surface quantity
$(\,)_{\text{PFC}}$	Propulsive fuselage concept quantity
$(\,)_{\text{ref}}$	Reference quantity
$(\,)_{\text{SC}}$	Side cylinder plane quantity
$(\,)_{\text{TP}}$	Trefftz plane quantity

the adoption of energy-based methodologies that provide more physically intuitive and analytically consistent interpretations (Sanders and Laskaridis, 2020; Drela, 2009; Arntz et al., 2015).

From an energy-based perspective, aircraft performance is evaluated via power terms rather than forces. This allows tracking of energy sources, sinks, and transfer pathways, offering a clearer understanding of loss mechanisms not captured by conventional analyses. Additional clarity is gained by adopting an absolute reference frame (ARF) (Sanders and Laskaridis, 2020; Sanders, 2023), in which the aircraft moves through a quiescent atmosphere, as opposed to the relative reference frame where the aircraft is stationary and flow passes over it. Despite their advantages, energy-based approaches have yet to see widespread adoption, and momentum-based analyses remain dominant in the evaluation of PFCs (Gray et al., 2018; Habermann et al., 2021; Battiston et al., 2021; Gray et al., 2020; Matesanz-García et al., 2022; Yildirim et al., 2022). This study addresses the limited application of energy-based methods, the lack of physical interpretability in existing performance assessments, and the absence of feature-specific flow decomposition in PFC evaluations.

An energy-based framework combined with flow feature decomposition is proposed to evaluate aero-propulsive performance in PFCs. Applied to a two-dimensional axi-symmetric model, this methodology enables systematic exploration of key design parameters including propulsor size, exhaust geometry, and nozzle shaping. To the authors' knowledge, this is the first study to apply energy-based flow feature segmentation to a large design space exploration of a BLI configuration and to offer a physically intuitive interpretation of work and energy relationships. These findings not only enhance the understanding of PFC aerodynamics but also suggest the use of energy-based quantities in geometry optimisation for better savings. In this work, we demonstrate how flow behaviours are modified when subject to design changes by using these quantities. The methodology is relevant to other disruptive aircraft architectures and can provide design insights.

2. Performance accounting approach

2.1. Enhanced mechanical energy balance

2.1.1. Mechanical energy balance

The mass, momentum and energy governing conservation equations derived in the ARF (Sanders, 2023) are applied to a short-to-medium range single-aisle reference aircraft to which a circumferential propulsor is integrated around the fuselage's tail. Two main engines mounted under-wing constitute a turbo-electrical and thrust-splitting aircraft architecture also commonly identified in the literature as a propulsive fuselage concept (PFC) (Moirou et al., 2023).

A two-dimensional section of the three-dimensional control volume, enclosed by bounding surface $\mathcal{S}$, is depicted in Fig. 1. The bounding surface is composed of an outer surface $\mathcal{S}_O$, represented as the side cylinder and Trefftz planes ($\mathcal{S}_O = \mathcal{S}_{\text{SC}} \cup \mathcal{S}_{\text{TP}}$), and an inner surface. The latter is further split into the fuselage and propulsor's nacelle walls, $\mathcal{S}_{\text{B}}$, and any permeable propulsive surfaces, $\mathcal{S}_{\text{P}}$ from $\mathcal{V}_{\text{P}}$ which contains the propulsor's internal working surfaces, such as the fan rotor and stator and flow passage. These internal surfaces can equally be represented by a volumetric body force model.

The direct application of the mechanical energy conservation equation to the control volume defined in Fig. 1 yields the mechanical energy balance (Moirou and Sanders, 2025) (or power balance). The

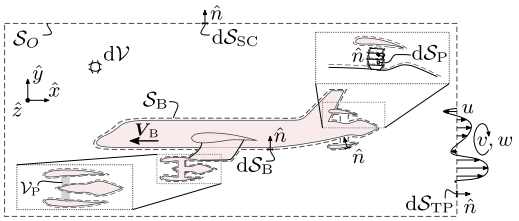


Fig. 1. Schematic of a control volume encapsulating a powered aerodynamic body.

terms are rearranged such that the left-hand side of Eq. (1) characterises the power sources to the flow, and the right-hand side the sinks:

$$\underbrace{-\oiint_{\mathcal{S}_{\mathrm{P}}}\left(p_{\mathrm{G}}\boldsymbol{V}'_{\mathcal{S}}-\bar{\bar{\tau}}\cdot\boldsymbol{V}'_{\mathcal{S}}\right)\cdot\,\mathbf{d}\mathcal{S}}_{\mathcal{P}_S}+\underbrace{\iiint_{\mathcal{V}}\rho\boldsymbol{f}\boldsymbol{V}'\,\mathrm{d}\mathcal{V}}_{\mathcal{P}_f}$$
$$\overbrace{+\underbrace{\oiint_{\mathcal{S}_{\mathrm{B}}}\left(p_{\mathrm{G}}\boldsymbol{V}_{\mathrm{B}}-\bar{\bar{\tau}}\cdot\boldsymbol{V}_{\mathrm{B}}\right)\cdot\,\mathbf{d}\mathcal{S}}_{-\mathcal{F}_{\mathbf{B}}\cdot\boldsymbol{V}_{\mathbf{B}}}+\underbrace{\iiint_{\mathcal{V}}\rho\boldsymbol{f}\boldsymbol{V}_{\mathrm{B}}\,\mathrm{d}\mathcal{V}}_{-\mathcal{F}_f\cdot\boldsymbol{V}_{\mathbf{B}}}}^{-\mathcal{W}h}=\cdots$$
$$\underbrace{-\oiint_{\mathcal{S}_O}\rho\frac{\boldsymbol{V}^2}{2}\boldsymbol{V}'+p_{\mathrm{G}}\boldsymbol{V}-\bar{\bar{\tau}}\cdot\boldsymbol{V}\cdot\,\mathbf{d}\mathcal{S}}_{\mathcal{E}}+\underbrace{\iiint_{\mathcal{V}}-p_{\mathrm{G}}\nabla\cdot\boldsymbol{V}\,\mathrm{d}\mathcal{V}}_{\Theta}$$
$$+\underbrace{\iiint_{\mathcal{V}}\left(\bar{\bar{\tau}}\cdot\nabla\right)\cdot\boldsymbol{V}\,\mathrm{d}\mathcal{V}}_{\Phi} \tag{1}$$

2.1.2. Propulsor mechanical power caveat

Mechanical power can either be represented with the amount of shaft power of the fan's rotor and blades through integration of the gauge pressure p_{G} and viscous stress tensor $\bar{\bar{\tau}}$ on the surfaces $\mathcal{S}_{\mathrm{P}}$ in the relative reference frame ($\mathcal{P}_S$), or a body force power ($\mathcal{P}_f$). Both quantities correspond to a rise in total enthalpy in the flow (ΔH) (Moirou and Sanders, 2025). Body force power is often favoured when the propulsor's geometry is unknown (Matesanz-García et al., 2022; Gray et al., 2020; Yildirim et al., 2022) where the volume-specific body force vector $\boldsymbol{f}$ is integrated in the relative reference frame. In the contrary, it is sometimes more convenient to model the propulsor as a set of inlet and outlet boundary conditions (BC) using $\mathcal{P}_S$.

That scenario echoes Drela's $\mathcal{P}_K$ term (Drela, 2009), to represent the change in mechanical energy flux between the inlet and outlet stations, on either side of the fan. However, there is a caveat regarding $\mathcal{P}_K$ because, unlike total enthalpy rise, its value will change according to the interface location of the inlet and outlet BC (Moirou and Sanders, 2025). This is because $\mathcal{P}_K$ inherently includes the pressure volume work, Θ_{P}, within the fan's volume, $\mathcal{V}_{\mathrm{P}}$, that is bound by the inlet and outlet interface planes. That rate of pressure work within the fan volume Θ_{P} is composed of an isentropic (reversible) component $\Theta_{\mathrm{rev,P}}$, and a non-isentropic (irreversible) one $\Theta_{\mathrm{irr,P}}$, echoing the Baroclinic power from Sato (2012) imparted to the flow and due to compressibility effects (Eq. (2)).

$$\mathcal{P}_S\equiv\mathcal{P}_f\equiv\Delta H\equiv\mathcal{P}_K+\Phi_{\mathrm{P}}+\Theta_{\mathrm{P}}=\underbrace{\mathcal{P}_K+\Theta_{\mathrm{rev,P}}}_{\mathcal{P}_K^*}+\underbrace{\Phi_{\mathrm{P}}+\Theta_{\mathrm{irr,P}}}_{\Phi_{\mathrm{P}}^*} \tag{2}$$

The corrected additional power $\mathcal{P}_K^*$ accounts for the local reversible portion of Θ within $\mathcal{V}_{\mathrm{P}}$ that will cancel out with the reversible portion of Θ in the surrounding external volume. Noting that $\Theta_{\mathrm{irr,P}}$ and Φ_{P} represent the fan's internal losses, they can be related to the fan's isentropic efficiency (Moirou and Sanders, 2025).

2.1.3. Work-energy transfers in flight

A plausible change in potential energy in Eq. (1) is introduced with $\mathcal{W}\dot{h}$ whereby any excess or deficit in power in the system would respectively result in climb or descent, with the rate-of-change in altitude $\dot{h}$. This potential energy-rate equates the pseudo-work rate of forces that act on the flow. As the term can either be positive or negative, it can be placed on either side of Eq. (1), whereby the descent of the aircraft would impart energy to the atmosphere through conversion of its potential energy.

The mechanical energy fluxes $\dot{\mathcal{E}}$ (Eq. (3)) crossing over the outer boundary surface $\mathcal{S}_O$, expressed in the ARF, can conveniently be decomposed into the side cylinder and Trefftz plane surfaces, $\dot{\mathcal{E}}_{\mathrm{SC}}$ and $\dot{\mathcal{E}}_{\mathrm{TP}}$ respectively, following Fig. 1 conventions. As a whole, $\dot{\mathcal{E}}$ is constituted of the wake stream-wise kinetic energy deposition rate $\dot{\mathcal{E}}_u$, the transverse kinetic energy deposition rate $\dot{\mathcal{E}}_v$, and the rates of wake pressure-defect work $\dot{\mathcal{E}}_p$, viscous boundary work $\dot{\mathcal{E}}_\tau$ and wave-outflow energy deposition $\dot{\mathcal{E}}_w$. Additionally, $\dot{\mathcal{E}}_u$ and $\dot{\mathcal{E}}_v$ sum up to $\dot{\mathcal{E}}_k$ characterising the overall wake kinetic energy deposition rate.

$$\dot{\mathcal{E}}=\overbrace{\underbrace{\iint_{\mathcal{S}_{\mathrm{TP}}}\left(\frac{\rho}{2}\boldsymbol{V}^2\right)\boldsymbol{V}'\cdot\hat{n}\,\mathrm{d}\mathcal{S}}_{\dot{\mathcal{E}}_k}+\underbrace{\iint_{\mathcal{S}_{\mathrm{TP}}}p_{\mathrm{G}}\boldsymbol{V}\cdot\hat{n}\,\mathrm{d}\mathcal{S}}_{\dot{\mathcal{E}}_p}+\underbrace{\iint_{\mathcal{S}_{\mathrm{TP}}}-\bar{\bar{\tau}}\cdot\boldsymbol{V}\cdot\hat{n}\,\mathrm{d}\mathcal{S}}_{\dot{\mathcal{E}}_\tau}}^{\dot{\mathcal{E}}_{\mathrm{TP}}}$$
$$+\overbrace{\underbrace{\iint_{\mathcal{S}_{\mathrm{SC}}}\left[\left(\frac{\rho}{2}\boldsymbol{V}^2\right)\boldsymbol{V}'+p_{\mathrm{G}}\boldsymbol{V}-\bar{\bar{\tau}}\cdot\boldsymbol{V}\right]\cdot\hat{n}\,\mathrm{d}\mathcal{S}}_{\dot{\mathcal{E}}_w}}^{\dot{\mathcal{E}}_{\mathrm{SC}}} \tag{3}$$

At the outer boundaries (SC and TP), only the excess in kinetic energy fluxes are captured, if both surfaces are defined sufficiently far from the body such that they do not experience pressure perturbations from the free-stream flow. The energy initially deposited within the flow $\mathcal{V}$ is eventually converted into other forms as represented by the sinks Θ_{irr} and Φ. This energy transfer takes place in the flow as it tries to resume to its initial quiescent state. The volumetric pressure work rate Θ is measured as the fluid experiences compression and dilation waves against the atmospheric pressure. It is analogous to Drela's power balance term $\mathcal{P}_V$, to which a notional split into irreversible and reversible was not present in their former definition. The last term of Eq. (1) Φ represents the accumulation rate in viscous dissipation along the flow path that manifests itself as heat and measures the irreversible mechanical losses. When measured at the Trefftz plane (TP) to capture all losses from the system, Φ and Θ are preferably referred to as Φ_∞ and Θ_∞.[1]

Alternatively, the mechanical energy balance can be written under a non-dimensional form using the free-stream dynamic pressure power. This non-dimensionalisation reduces to coefficients $C_{\mathcal{X}}$, where $\mathcal{X}$ can take the form of any term from the balance. Nonetheless, to not depend on the reference surface area $\mathcal{S}_{\mathrm{ref}}$ selected, the term is preferred on the left-hand side of the equation. That form of Eq. (4) enables the comparison of specific terms $\mathcal{X}$ between different configurations, e.g. sizes or designs.

$$C_{\mathcal{X}}\,\mathcal{S}_{\mathrm{ref}}=\frac{\mathcal{X}}{\frac{1}{2}\rho_\infty V_\infty^3} \tag{4}$$

2.2. Application to decoupled aero-propulsive partial assemblies

To simplify the analysis, weak aerodynamic coupling is assumed between the fuselage assembly (fuselage and thruster) and the remaining aerodynamic components (wings, pylons, under-wing engines and

[1] This notation is only used when the Trefftz plane is located very far downstream.

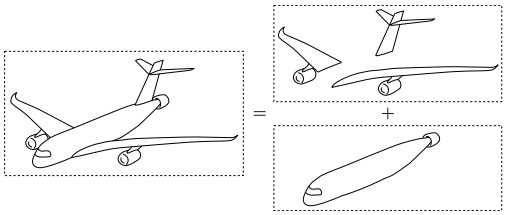


Fig. 2. Decomposition of the propulsive fuselage concept into partial assemblies: fus+P at bottom and rest at top.

vertical and horizontal tail planes) via an approach similar to a drag build-up method (Fig. 2) (Moirou and Sanders, 2025). In doing so, the fuselage assembly experiences a net force imbalance $\boldsymbol{\mathcal{F}}_{\mathbf{imb}}$, even in steady-level flight condition, which must be accounted for within the energy balance (Moirou and Sanders, 2025).

This formulation becomes advantageous as it allows a problem simplification by isolating a system and evaluate its performance. To that end, $\boldsymbol{\mathcal{F}}_{\mathrm{imb}}$ is quantified with an explicit formulation of forces imbalance over partial assemblies (fuselage, $\boldsymbol{\mathcal{F}}_{\mathrm{fus}}$, and BLI propulsor, $\boldsymbol{\mathcal{F}}_{\mathrm{P}}$), and proves its usefulness when thrust-splitting architectures are considered to deduce the remaining force necessary by the under-wing engines to maintain the net change in potential energy of the entire aircraft. In these scenarios, the energy balance in Eq. (1) reduces to Eq. (5) where the net potential energy change is substituted with its sub-assembly quantity, related to an imbalance force.

$$\mathcal{P}_S + \mathcal{P}_f - (\boldsymbol{\mathcal{F}}_{\mathrm{fus}} + \boldsymbol{\mathcal{F}}_{\mathrm{P}}) \cdot \boldsymbol{V}_{\mathrm{B}} = (\dot{Wh})_{\mathrm{rest}} + \dot{\mathcal{E}} + \boldsymbol{\Phi} + \boldsymbol{\Theta} \tag{5}$$

2.3. Flow feature decomposition

Within the flow, different features are identifiable leading to different flow mechanisms and better flow assessments. Following the different flow feature identification methods reviewed by Moirou et al. (2023) and the flow decomposition precedence introduced by Sanders (2018), main and sub features are extracted in this work as given by Fig. 3.

2.3.1. Flow decomposition precedence procedure

The viscous layers represented with the main boundary layer forming over the fuselage, the secondary boundary layer developing over the propulsor cowl, and their subsequent wake, are identified along with the wave-induced losses and the jet plume using the following method:

- The viscous portion of the flow is first extracted from the computed flow solution as per defining the amount of mass-flow ingested by the propulsor relative to the amount of mass-flow contained within the BL. The shear identifier ξ introduced by Sanders and Laskaridis (2020) is followed whereby each cell is contrasted against the volume integral of the quantity to define a threshold value. The shear layer encompasses both boundary layers (the main and secondary), as well as the wake that starts downstream of the vehicle's nacelle.

$$\xi = \left(\frac{\mu + \mu_t}{\mu}\right) \frac{\left(\nabla \cdot \bar{\bar{\tau}}\right) \cdot V}{|p\nabla \cdot V|} > \frac{1}{\mathcal{V}} \iiint_{\mathcal{V}} \xi \, \mathrm{d}\mathcal{V} \tag{6}$$

- The shock-waves that might form over the propulsor cowl or the fuselage are identified by ζ in Eq. (7) from the work done by Lovely and Haimes (1999) with a cut-off value of 0.95 based on the recommendations from Sanders and Laskaridis (2020) and Arntz and Hue (2016). Despite the difficulties to isolate the shock regions, the approach is robust enough to isolate them even though Arntz and Hue (2016) suggests an improved method. The user input requirement is not suitable in this work as a large design exploration is performed.

$$\zeta = \frac{V \cdot \nabla p}{a\,|\nabla p|} > 0.95 \tag{7}$$

- The jet plume is extracted from Υ with Eq. (8) where previous sensitivity studies have been conducted by Sanders and Laskaridis (2020). The jet plume is isolated by means of total enthalpy deviation accounting for a 10% rise in the quantity downstream of the propulsor. The jet plume is anticipated to attenuate the wake region of the flow whereby additional features are identified and isolated.

$$\Upsilon = \left|\frac{\Delta H - H_\infty}{H_\infty}\right| > 1.10 \tag{8}$$

A step further into the flow breakdown emphasises on the different features confined within the propulsor jet. The flow characteristics are obtained following the precedence procedure on the isolated plume:

1. The jet region is extracted with Υ for a neat separation between the plume and its surrounding flow. Within its volume, a succession of compression and dilation waves form and identify the core of the plume.
2. The sub-region of the jet experiencing strong compression is identified with the core-compression filter ζ. Even though the shocks are filtered-out of the jet-flow, the delay imparted in viscous dissipation does not allow a fair quantification.
3. The previously used ξ identifier leaves behind the jet/wake mixing volume, or viscous attenuation, from the pure jet, i.e. jet-core. The highly dissipative nature of the mixing volume is isolated from the jet-stream leaving behind a purely isentropic expansion process, described as the core-expansion.

2.3.2. Main features

First, the main features are represented by their associated power losses on the left hand side of Fig. 3 and obtained following the procedure above: the boundary layers (BL and nac), the wake (WK), the shock waves (SW) and the jet plume (JET). However, there is a caveat in the local decomposition of the total mechanical loss. While the rate of viscous dissipation $\boldsymbol{\Phi}$ is a positive-only quantity, the rate of volumetric pressure work $\boldsymbol{\Theta}$ can locally take positive or negative values. The separation of $\boldsymbol{\Theta}$ into its isentropic and non-isentropic parts attributes respectively a recoverable constituent, and an irreversible loss. Although it is easier to assess only the viscous dissipation rate on the segmented flow regions, the irrecoverable losses can all be lumped together in a mechanical loss term $\boldsymbol{\Phi}^*$ under the form of Eq. (9) where a bulk flow quantity $\boldsymbol{\Phi}^*_{\mathrm{bulk}}$ is added to quantify the losses not captured numerically by the different identifiers.

$$\boldsymbol{\Phi}^* = \boldsymbol{\Phi}^*_{\mathrm{BL}} + \boldsymbol{\Phi}^*_{\mathrm{nac}} + \boldsymbol{\Phi}^*_{\mathrm{WK}} + \boldsymbol{\Phi}^*_{\mathrm{SW}} + \boldsymbol{\Phi}^*_{\mathrm{JET}} + \boldsymbol{\Phi}^*_{\mathrm{bulk}} \tag{9}$$

To consider the volumetric pressure work $\boldsymbol{\Theta}$, an exact tracking is enabled by only considering the irreversible component $\boldsymbol{\Theta}_{\mathrm{irr}}$. Sato (2012) introduced $\boldsymbol{\Phi}^*$ as the sum of all energy forms within a feature however, this can double account for quantities that are in the form of available energy in a volume and transformed into another form in another feature, e.g. the BL kinetic energy dissipated in the wake. Therefore, it becomes pragmatical to only track the progress of viscous dissipation and irrecoverable volumetric pressure work rates, as defined with Eq. (10), adopting the notation introduced by Sato.

$$\boldsymbol{\Phi}^* = \boldsymbol{\Phi} + \boldsymbol{\Theta}_{\mathrm{irr}} \tag{10}$$

2.3.3. Jet plume partitioning

The precedence procedure successfully demonstrates the decomposition of the various flow mechanisms present in BLI and allows $\boldsymbol{\Phi}^*_{\mathrm{JET}}$ to be decomposed into its core-compression (CC), core-expansion (CE) and jet/wake mixing (MIX) regions (Eq. (11)). The advantage of this

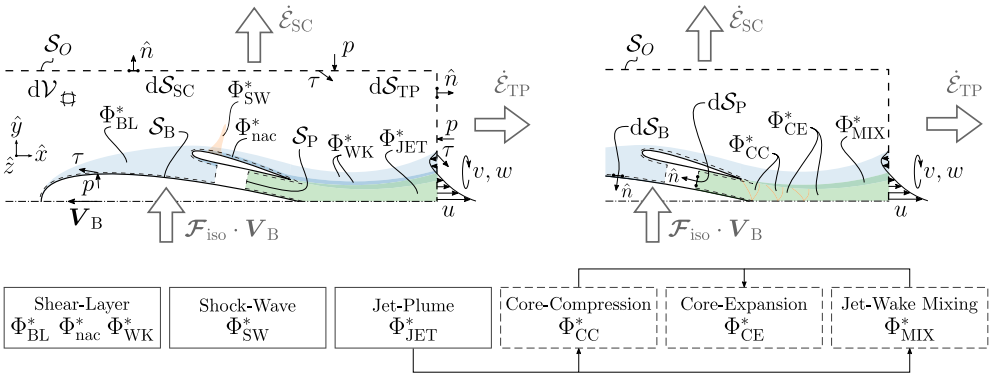


Fig. 3. Flow-chart of the precedence process for work flow-paths identification and schematic of the corresponding mechanisms.

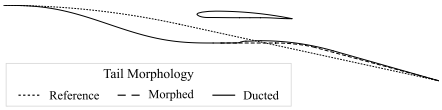


Fig. 4. Morphing sequence of a rear-mounted BLI propulsor from its reference and morphed tail fuselages.

application is the quantification of the individual contributions to the overall benefits, whether in form of viscous dissipation or irreversible pressure work.

$$\boldsymbol{\Phi}^*_{\mathrm{JET}} = \boldsymbol{\Phi}^*_{\mathrm{CC}} + \boldsymbol{\Phi}^*_{\mathrm{CE}} + \boldsymbol{\Phi}^*_{\mathrm{MIX}} \tag{11}$$

Nevertheless, with the consideration of BCs to model the propulsor blades and its stage in computational fluid dynamics (CFD), detailed later, large contributions of pressure work and viscous dissipation rate are neither solved or captured. To prevent the use of the Θ decomposition in its isentropic and non-isentropic components, which still needs to be proven and validated, the analysis entirely focus on the viscous dissipative losses $\boldsymbol{\Phi}$. The inclusion of Θ_{irr} is thus left for consideration in further work.

Finally, following the flow-paths of the system, the mechanical energy balance on partial assemblies is re-written accounting for all flow mechanisms in Eq. (12).

$$\begin{aligned}\mathcal{P}_S + \mathcal{P}_f + \left(\boldsymbol{\mathcal{F}}_{\mathrm{fus}} + \boldsymbol{\mathcal{F}}_{\mathrm{P}}\right)\cdot \boldsymbol{V}_\infty = (W\dot{h})_{\mathrm{rest}} + \dot{\mathcal{E}} + \boldsymbol{\Phi}^*_{\mathrm{BL}} + \boldsymbol{\Phi}^*_{\mathrm{nac}} + \boldsymbol{\Phi}^*_{\mathrm{SW}} + \boldsymbol{\Phi}^*_{\mathrm{WK}} \\ + \underbrace{\boldsymbol{\Phi}^*_{\mathrm{CC}} + \boldsymbol{\Phi}^*_{\mathrm{CE}} + \boldsymbol{\Phi}^*_{\mathrm{MIX}}}_{\boldsymbol{\Phi}^*_{\mathrm{JET}}} + \boldsymbol{\Phi}^*_{\mathrm{bulk}} + \Theta_{\mathrm{rev}}\end{aligned} \tag{12}$$

2.4. Aero-propulsive performance assessment

To relate the flow mechanisms through their flow-paths to the overall aero-propulsive performance of the PFC, the approach developed by Moirou and Sanders is used (Moirou and Sanders, 2025). The reference aircraft is defined following a drag build-up approach to indicate the propulsive force requirement from the under-wing engines. Its isolated fuselage axial net force (indicated as "Reference" in Fig. 4), $\mathcal{F}_{\mathrm{fus,ref}}$, is evaluated via CFD and related back to the overall aircraft drag $\mathcal{F}_{\mathrm{A/C,ref}}$. Stemming from the reference aircraft, a reference morphed fuselage geometry is derived ("Morphed" in Fig. 4) to provide an improved understanding of the integration effects from the aft-mounted propulsor. Subsequently, the net force on this PFC isolated fuselage is also evaluated from CFD with $\mathcal{F}_{\mathrm{fus,PFC}}$. To extract the force contribution from the BLI propulsor, the net axial force ($\mathcal{F}_{\mathrm{fus+P,PFC}}$) on the PFC ("Ducted" from Fig. 4) is determined from *near-field* integration over the vehicle in CFD.

It is stressed that thrust is used as a notional quantity and should represent useful work, or the forward contribution of the force distribution over the aerodynamic body. In that respect, propulsive force is preferred to thrust where the thruster contribution in the PFC is characterised with a propulsive force share (PFS). Assuming that the remaining force requirement is provided by the under-wing propulsion systems to maintain a steady cruise condition, the numerator is obtained from the difference between the powered PFC and unpowered morphed fuselages:

$$\mathrm{PFS} = \frac{\mathcal{F}_{\mathrm{fus+P,PFC}} - \mathcal{F}_{\mathrm{fus,PFC}}}{\mathcal{F}_{\mathrm{PFC}}} \tag{13}$$

The energy harvested by the BLI propulsor from the flow reduces the power demand from the fan required to achieve the configuration's desired net force. These benefits are quantifiable with a power saving coefficient (PSC) by means of comparison between the novel aircraft and its reference. As the thrust-splitting architecture distributes the thrust requirement to the BLI propulsor and under-wing turbofans, combinations of PFS and PSC can be used to target the best compromise. Although the BLI propulsor power $\mathcal{P}_{S,\mathrm{P}}$ is extracted from CFD at the specific force contribution, the power supply from the under-wing power-plants to the thruster $\mathcal{P}_{\mathrm{P}}$ is used to be related to a transmission system's efficiency η_{trans}. Additionally, the power consumed by the under-wing engines to generate thrust needs to be modelled in both the PFC and reference aircraft (Section 3.1). As such, the podded engines (POD) define $\mathcal{P}_{\mathrm{A/C,ref}}$ for the reference model and are coupled with the thruster to define the PFC total power consumption $\mathcal{P}_{\mathrm{PFC}}$.

$$\mathrm{PSC} = \frac{\mathcal{P}_{\mathrm{A/C,ref}} - \mathcal{P}_{\mathrm{PFC}}}{\mathcal{P}_{\mathrm{A/C,ref}}} = 1 - \frac{\mathcal{P}_{\mathrm{POD}} + \mathcal{P}_{\mathrm{P}}}{\mathcal{P}_{\mathrm{A/C,ref}}} = 1 - \frac{\mathcal{P}_{\mathrm{POD}} + \frac{\mathcal{P}_{S,\mathrm{P}}}{\eta_{trans}}}{\mathcal{P}_{\mathrm{A/C,ref}}} \tag{14}$$

To maximise PSC, it is essential to minimise the power demand from the BLI propulsor and under-wing podded engines by ensuring the most efficient utilisation of available energy. This requires reducing energy losses within the flow, specifically in the forms of Θ_{irr} and $\boldsymbol{\Phi}$. Consequently, this study emphasises on tracking these two quantities to establish a direct relationship with PSC and overall efficiency.

3. Propulsive fuselage concept design

In this work, a two-dimensional axi-symmetric approximation of a PFC is considered to reduce the computational demand. This lower order modelling constrains the degrees of freedom for a design space exploration (DSE) but still allows one to investigate the influence that many macro parameters have on the surrounding flow-field, and therefore the vehicle performance. In the same vein as the NASA STARC-ABL (Welstead and Felder, 2016) and the CENTRELINE (Seitz et al., 2018) projects, a conventional single-aisle short-to-medium range aircraft is morphed into a PFC to accommodate an aft-integrated propulsor.

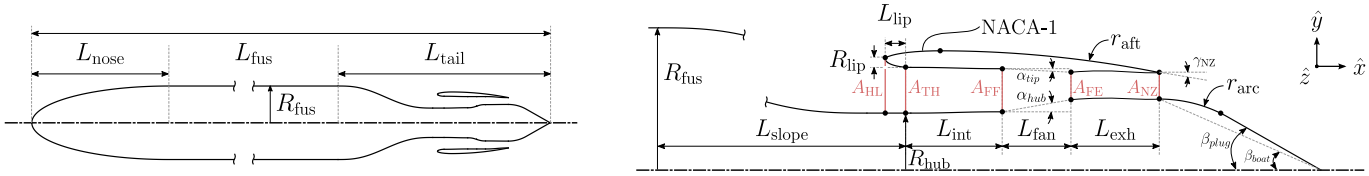


Fig. 5. Schematic of an axi-symmetric fuselage with a thruster, with its tail slope, propulsor intake, cowl, exhaust, and aft-cone geometries parametrisation (black) and thermodynamic stations (pink). (For interpretation of the references to colour in this figure legend, the reader is referred to the web version of this article.)

3.1. Reference aircraft

A conventional short-to-medium range aircraft is used as reference to derive an axi-symmetric body of revolution lacking wings, belly fairing, empennage and stabilisers. Its approximation is based upon a drag build-up approach (Moirou and Sanders, 2025) where the fuselage is isolated as a 2D axi-symmetric aerodynamic body computed in CFD and whose net body force is related back to the overall aircraft propulsive force requirement to maintain a steady-level flight (Moirou et al., 2024).

To benchmark the relative performance of the propulsive fuselage concepts over the reference, and assess the BLI benefits, the reference aircraft is propelled in two different ways: with a fictitious propulsion system of propulsive efficiency of 100% and with state-of-the-art turbofan engines (Moirou et al., 2024; Zhao and Yao, 2022).

Based on state-of-the-art propulsion systems propelling short-to-medium range aircraft, e.g. CFM LEAP-1 or PW1100G, a two-spool turbofan architecture is selected and developed by Zhao and Yao (2022). The engine is composed of an 11:1 by-pass ratio single-stage fan (with a pressure ratio of 1.49), 3-stage intermediate-pressure and 10-stage high-pressure compressor driven by a 2-stage high-pressure and 7-stage low-pressure turbines for an overall pressure ratio of 44.

3.2. Propulsive fuselage concept

3.2.1. Morphing sequence

While a convenience exists in retrofitting a BLI propulsor around a conical tail[2] (Sanders, 2018), other considerations favour reshaping the fuselage tail to accommodate better the propulsor. This allows the flow to enter the BLI fan axially whereas the retrofit places constraints on the nacelle design, which incur losses due to separation over the aft body of the nacelle (Sanders, 2018; Moirou et al., 2024). By allowing the tail to be morphed, one can relax this constraint and mitigate those losses. However, this introduces new trade-offs with possible flow separation ahead of the intake due to the serpentine curve, as well as behind the propulsor because of steep plug angles (Moirou et al., 2024).

The sequence from the reference tail to its ducted reshaped form is illustrated in Fig. 4. In the same vein as an existing concept (Seitz et al., 2018), this design favours a serpentine pre-inlet outline in lieu of a tapered slope (Welstead and Felder, 2016). While an adequate diffusion must be ensured for the flow to enter the BLI fan, it can either be done with a pre-diffusion, an internal diffusion within the intake, or a combination of both. For an efficient fan operation with a suitable Mach number at the fan-face, and to prevent separation upstream of the thruster, and recirculation behind the fuselage, a nominal position of the propulsor is down-selected from Moirou et al. (2024).

Despite the rather simple representation in Fig. 5, the design variables defined allow one to explore the rear-end design space (exhaust and plug) and the propulsor size and pressure ratio simultaneously, while evaluating their influence on the aero-propulsive performance.

3.2.2. Aerodynamic and propulsive modelling

An automated structured grid generation methodology is implemented using ANSYS ICEM 20.2 (ANSYS, Inc., 2020b). All geometries are encapsulated by bullet-shape domains following a multi-block strategy. The multi-grid structure is composed of a C-grid topology surrounding the vehicle from its centreline, with a second C-grid topology to refine the nacelle and propulsor region (Fig. 6). To avert flow impingements to the far-field, a coupled grid and domain convergence study advised on 10 fuselage chords upstream and above the body $d_{\text{far-field}}$, and a Trefftz position d_{outlet} at 40 fuselage lengths behind it (Moirou and Sanders, 2025). The mesh parametrisation is elaborated in a fashion that elements close to the wall ensure a fineness with a y^+ that falls between 0.9 and 1.0 along the whole body, and coarsen by a certain coefficient the farther away from the vehicle, with a capped value as it approaches the domain's outlet. For the geometries considered in this work, the grid is around half a million elements (Moirou and Sanders, 2025), giving grid convergence indices (GCI) of 0.01 and 0.02% and an error between *near-field* and *far-field* field forces of −0.27%.

The flow-field is numerically solved using the density-based Reynolds-Averaged Navier–Stokes equations in ANSYS Fluent 2020R2 (ANSYS, Inc., 2020a). The Shear-Stress Transport (SST) k-ω turbulence model (Habermann et al., 2021; Matesanz-García et al., 2022) is selected with second-order spatial discretisation and no-slip condition over the walls, whereas the far-field conditions are modelled with a pressure far-field upstream the body (flight level FL350, $M = 0.78$ and $Re = 2.73.10^8$ at ISA conditions) and a pressure outlet condition at the exit plane (Fig. 7). Caution is nonetheless highlighted on the turbulence model as it is challenged by the eddy-viscosity assumption.

From the low-pressure shaft, power is extracted to feed the thruster via a black-boxed system where a transmission efficiency is applied to the system ($\eta_{trans} = 100\%$ herein). The BLI propulsor is then modelled in CFD using BC following an iterative procedure where the fan-face is accounted as a pressure outlet whereby a static pressure and a target mass-flow rate are provided. To set a technology level, a fan polytropic efficiency target is defined. Ensuring continuity through the fan stage, the fan-exit is defined as a mass-flow inlet. An iterative procedure between the fan-face flow properties, fan pressure ratio (FPR) and polytropic efficiency ensures a correct mass-flow averaged total temperature with a monitoring of the convergence of the relative difference in FPR, polytropic efficiency and mass-flow imbalance.

Relative to the reference aircraft, the on-board engines of a PFC can be down-scaled as their thrust requirements reduce, enlarging the savings. Nonetheless, in this study the reference engine at its size is conserved (retrofitting) operating at off-design for different power off-take and force requirements. Previous work as shown that extra 5% savings can be achieved when resizing the main turbofans (Moirou et al., 2024).

[2] The convenience lies in closer comparisons between the BLI and reference aircraft, because the fuselage geometry is equivalent.

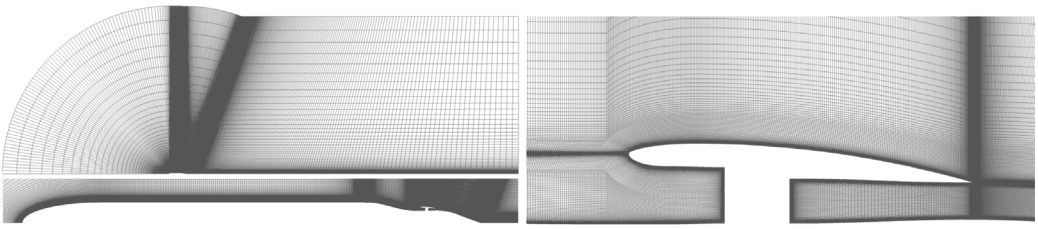


Fig. 6. Coupled C-structure grid around a propulsive fuselage with the mesh of the domain, around the fuselage and around the propulsor.

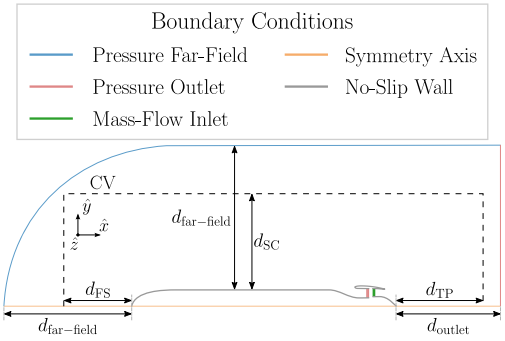


Fig. 7. Schematic of the domain, propulsive fuselage model, boundary conditions and analysis control volume.

3.3. Design space sampling

The exhaust and nozzle DSE is performed through combinations of parametric studies with variations in nacelle trailing edge droop angle, γ_{NZ}, plug angle, β_{plug} and hub and tip hade angles, α_{hub} and α_{tip}, respectively. These parameters are qualified as macro in this work as they allow to change the shape of the propulsor exhaust, direct the outflow, change the plug cone shape and the nacelle aft-end cowl (Moirou, 2023).

The deviations in nacelle droop are described as relative radial positions from the nacelle leading edge radius, $\Delta_{\text{nac,TE}}$, in preference to the nacelle trailing edge (TE) droop angle, γ_{NZ}. This coefficient multiplies the throat radius to define the radius offset between the leading and trailing edges radial positions, and is preferred because of the scaling experienced by the nacelle as the throat height increases to ingest more mass-flow. The droop angle is altered as the nacelle scales up or down whereas the relative position of the TE is unchanged, facilitating comparison between designs of different sizes.

The hade angles defined at the fan hub and tip describe the angles between the fan-face and fan-exit stations (Walsh and Fletcher, 2004) and entail changes in the exhaust starting points, hence shapes. For conciseness, only the hub hade angle is reported within the results but it is stressed that the designs are generated in pairs with a difference of 10° between the angles, i.e. $\alpha_{hub} = 10°, 5°, 0°$ and $\alpha_{tip} = 0°, -5°, -10°$ respectively.

Lastly, from the reference airframe boat-tail angle β_{boat}, derivatives are generated with the plug angle β_{plug} (Fig. 5) which inherently adjusts the circular arc radius r_{arc} and chord, thus length, to ensure continuity and tangency at the nozzle plane and plug cone. To enable a comparison between designs, a non-dimensional plug angle coefficient is introduced as the ratio of the plug angle to that of the boat, $f_{plug} = \beta_{plug}/\beta_{boat}$.

To approach the exploration of the aft-mounted propulsor's design space, a clustered (i.e. grouped) quasi-systematic (i.e. quasi equally distributed) sampling is used. The population is clustered in combinations of propulsor sizes that ingest different amount of mass-flow subject to different fan pressure ratio (FPR). The throat height, or area, is represented with the non-dimensional boundary layer ratio (BLR) which allows comparison amongst the different geometries under equivalent flight conditions. The variable is computed as the ratio of ingested mass-flow rate at the throat thermodynamic station, where $x_{\text{TH}} = L_{\text{fus}} + (L_{\text{slope}} - L_{\text{tail}})$, over the mass-flow present in the entire BL of height δ that develops over the morphed un-installed fuselage at the same axial position, i.e. considering the fuselage contour without propulsor. This comparison provides a non-conservative estimation of the mass-flow rate through the propulsor (Moirou et al., 2024), but consistent amongst all geometries, from the un-installed fuselage as it excludes the interaction effects that are known to thicken the BL (Gray et al., 2018).

Subsequent to the clusterisation, a quasi-systematic seeding on the nacelle trailing edge droop, plug and hade angles is conducted, as given in Fig. 8. This corresponds in total to a population of 1350 geometries with 5 BLR, 5 FPR, 4 nacelle trailing edge droops, 3 hade angles combinations and 5 plug angles, discarding the unrealisable geometries due to the parametrisation, i.e. out of the 1500 possible design combinations.

4. Work-energy transfers in flight

The right-hand side terms of Eq. (5) show that energy transfer happens between $\dot{\mathcal{E}}$ and Φ and Θ. In this section, the impact of the propulsor size and operating conditions is demonstrated, as well as with the exhaust design parameters investigated. Additionally, the volumetric quantities are related back to the design changes.

4.1. Energy flux transfers precedence and dependencies

To understand how efficiently the provided power is converted between its different sources and losses, Fig. 9 quantifies the transfer of power in the flow region behind the aircraft, i.e. $x_{\text{TP}}/L_{\text{fus}} > 1$. The top row represents the decay of the mechanical energy present in the flow as it attempts to resume to its initial quiescent state, while the bottom row illustrates the accumulation of Φ and Θ during that process.

Notably, a rapid exchange takes places between the $\dot{\mathcal{E}}$ terms and Θ in response to the isentropic expansion within the jet plume. The remaining quantity of $\dot{\mathcal{E}}$ diminishes at a slower rate as a result of shear within the flow, represented by the accumulation of viscous dissipation Φ. The transfer processes suggest a precedence given to Θ. Interestingly, the left-over amount of energy appears more important for large FPR and increases with respect to the mass-flow that travels through the fan. This indicates that the surplus comes to a cost and diminishes returns, i.e. it lowers the savings offered by the configuration while not enhancing its propulsive performance.

To echo the fallacy presented on Θ, a BFM representation should invert the monotonicity observed whereby higher FPRs imply higher compression and higher local Θ shifting upward its quantity at $x_{\text{TP}}/L_{\text{fus}} = 1$. As the available energy is getting converted, the higher BLRs experience higher amounts of pressure work which residual quantity (non-isentropic) lies higher than for low BLR.

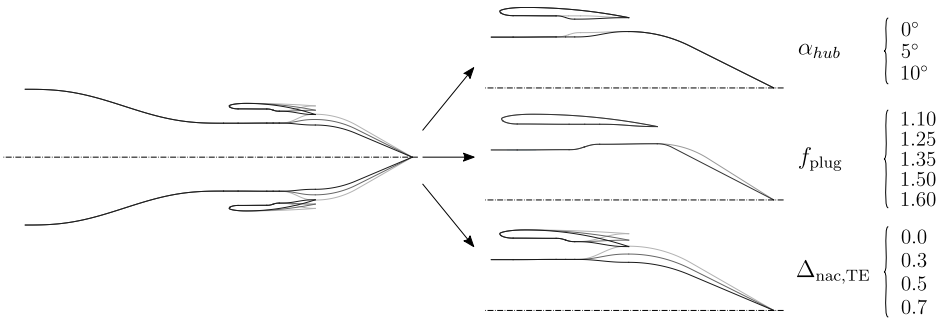


Fig. 8. Variations in the exhaust and plug design, following the design variables defined in Fig. 5.

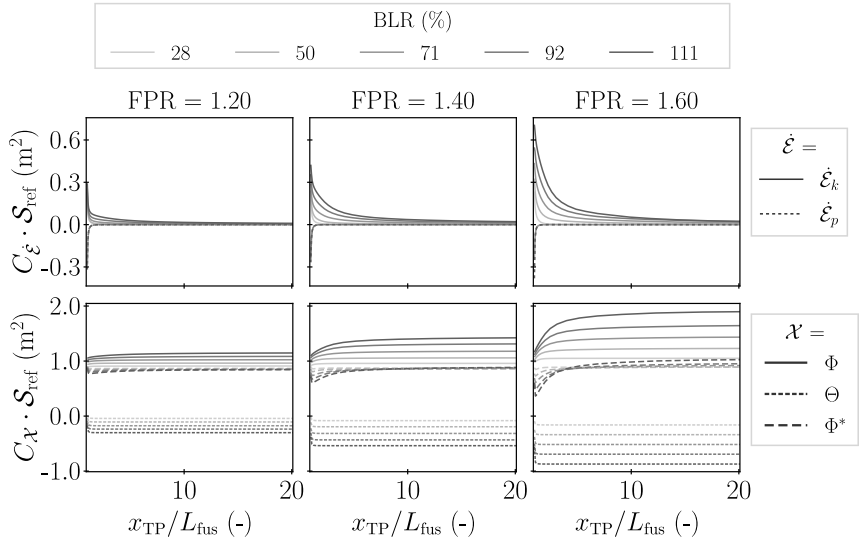


Fig. 9. Computed energy flux transfer between the kinetic energy deposition rate and the volumetric rate of viscous dissipation, pressure work and overall sink for various BLR and FPR.

4.2. Volumetric viscous dissipation and pressure work

The irreversibly lost energy that manifests itself as viscous dissipation can be characterised along with the volumetric pressure work. Fig. 10 illustrates the dependency of both these variables, Φ and Θ, and the total mechanical loss Φ^*, for the different BLR and FPR clusters.

Expectantly, Φ is correlated to BLR and FPR (Fig. 10(a)) which, as a coupled effect, increases at higher rates for larger combinations, as more work is provided to the flow from the fan. Through the expansion process within the jet plume, the overall pressure work (Fig. 10(b)) suggests a converse trend wherefrom larger amounts of mass-flow that go through the propulsor contribute greatly to the forward force production. Notwithstanding its greater contribution with respect to both BLR and FPR, the viscous dissipation still outweighs those benefits albeit flattening for lower FPR (Fig. 10(c)). An indication on the performance is therefore provided on the low FPR and high BLR propulsors which greatly contribute towards positive force (thrust direction) while not imparting more irrecoverable losses into the flow thanks to the expansion process. That combined increase therefore covers a larger PFS range (Fig. 10(d)) hence, suggesting optima to the lower-half range of PFS. The further increase in PFS results in irrecoverable loss which lowers the benefits claimed by the configuration.

While BLR is a natural parameter, as it is related to the amount of mass flow ingested, FPR is a result of the power provided by an external device. To apply the same FPR to a larger amount of mass-flow, it requires more energy that will be effectively used or lost. It appears therefore that a compromise must be found between these parameters to harvest all the possible energy available in the lower-viscous region of the BL while re-energising the remaining portion of the flow to generate a propulsive force at a low power cost.

It is important to stress that any increase in gauge static pressure results in a positive contribution in Θ which highlights a conspicuous caveat with respect to Θ. The highly compressible nature of the flow between the fan-face and face-exit presents a large positive contribution that is omitted by the BC used. Tse (2021) demonstrates the variation in $P_V = -\Theta$ between the propulsor inlet and varying outlet locations, which integrand presents a large positive contribution of Θ. Nonetheless, its proportion relative to the overall pressure work is yet to be defined, and is expected to depend on both BLR and FPR, which in other terms means that the replication of this study with a body-force model (BFM) rather than BC would impact the overall pressure work as well as the system's losses and thus impacts the benefits. Albeit being confined in the small region of the fan stage, it can be hypothesised that Θ should appear positive, and even greater with respect to both BLR and FPR. A physical interpretation could stand in the amount of mass-flow that is displaced by the amount of work imparted, echoing the displacement thickness defined in the BL properties.

Although being correct for the study herein presented, Φ^* looses its full meaning because of the misleading interpretation that follows Θ with BC. As such, Φ is favoured to characterise the performance of the system from a reduction of its quantity, i.e. a reduction in dissipation insinuates a better use of the provided power and hence a better performance as Φ is a positive-only term. However, it could be argued that the fan contribution to Φ is also missing but that would not change the trends obtained in Fig. 10 albeit increasing their growth gradients.

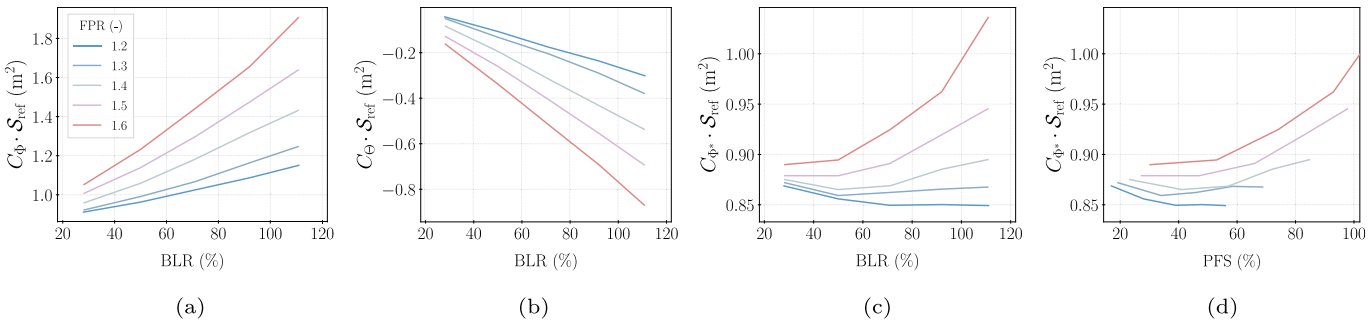


Fig. 10. Computed volumetric rate of (a) viscous dissipation, (b) pressure work, and overall losses as a function of (c) BLR and (d) PFS.

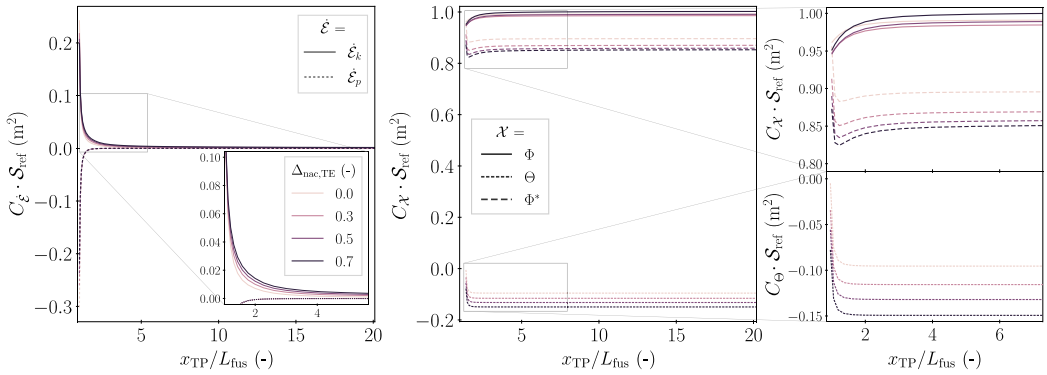


Fig. 11. Computed energy flux transfer between the kinetic energy deposition rate and the volumetric rate of viscous dissipation, pressure work and overall sink as a function of the nacelle droop.

4.3. Influence of the nacelle design on the energy transfers

A focus on the exhaust design space exploration shows the influence of the hade, plug and droop angles in energy transfers. However, due to the subtle variations in hade and plug angles, quasi-insensitive transfers are reported and therefore, only the droop influence is depicted in Fig. 11 for the BLR and FPR combination of the best performing candidate (BLR = 50% and FPR = 1.30) (Moirou et al., 2024) and its hade and plug angles.

Starting with the nacelle trailing edge that is mounted-flush with its front-end ($\Delta_{nac,TE} = 0.0$), the available energy $\dot{\mathcal{E}}$ is less effectively used as given by the highest dissipation (for a given fan energy deposition rate). It is noted that the penalty in additional dissipation is caused upstream of the vehicle's trailing edge, meaning that losses occur within the exhaust or along the plug. By embedding further the nacelle rear-end into the fuselage tail, it is observed the same precedence for Θ which remaining energy flux dissipates from shear. However, it is noted that while the three lowest $\Delta_{nac,TE}$ dissipate a roughly similar amount of energy Φ at $x_{TP}/L_{fus} = 20$, a better utilisation of the energy is obtained for the middle design of the three. An explanation lies in the amount of energy that has dissipated just downstream of the propulsor. At $x_{TP}/L_{fus} = 1$, Φ of both $\Delta_{nac,TE} = 0.3$ and 0.5 are smaller than for 0.0 and 0.7 indicating better designs between the fan-exit and the fuselage end-point. As for Θ, it is fair to assume that the pressure work is identical upstream of the fan at constant BLR and just downstream at the same FPR. The difference reported at $x_{TP}/L_{fus} = 1$ thus suggests a larger expansion process that occurs within the exhaust and upstream of the trailing edge and hence contributing to a higher performance as the flow leaves the rearward facing plug surface.

To summarise, this confirms that higher BLR and FPR are responsible for larger quantity of dissipation and pressure work (Fig. 9), but that these are also affected by the exhaust/nozzle design.

4.4. Energy loss mitigation via tailoring plug and nacelle trailing edge geometry

The comparison of the viscous dissipation and pressure work for all vehicles designed at BLR = 50% and FPR = 1.30 is given in Fig. 12. The changes in droop and plug angles non negligibly allow the design to be further refined to attenuate the losses occurring in the flow. Notably, the comparison between the different designs and the best performer, defined as datum, highlights the importance of both angles. At a given nacelle TE droop, smoothening the circular arc of the plug and increasing the steepness of the plug downstream of it enhances the shear stress and the viscous dissipation, and conversely, an abrupt plug cone reduces the viscous loss. This observation however cannot be generalised and only applies to the investigated size as the mass-flow rate and pressure rise are reasonably low, allowing the flow to remain attached to the plug wall surface.

Despite the ±2% error on FPR, the trends remain similar whereby penalties in forward force are obtained for mounted-flush nacelle trailing edges and increase with large plug angles. Intrinsically, this does not only affect the forward force but also the irrecoverable loss, power consumption and hence savings.

At constant power addition $\mathcal{P}^*_K$, any change in the losses Φ results in changes in either Θ or $\dot{Wh}$ to match a specific net force or would otherwise generate a force imbalance that will be represented by the PFS (Fig. 12). It has been seen in Fig. 10 that the coefficients do not have the same amplitude and therefore the relative differences depicted here do not have the same extents. There is a caveat in the absolute value and relative difference in Θ but it is nonetheless fair to assume that apart from the local pressure gradient difference that arise from changes in design, Θ should be constant up to the fan stage. To relate its quantity to the performance, its value must be positive and as low as possible. However, the sum of smaller Φ and Θ implies smaller net force whereas it also exists combinations of smaller, or greater, Φ and Θ which indicate a change in rate of potential energy.

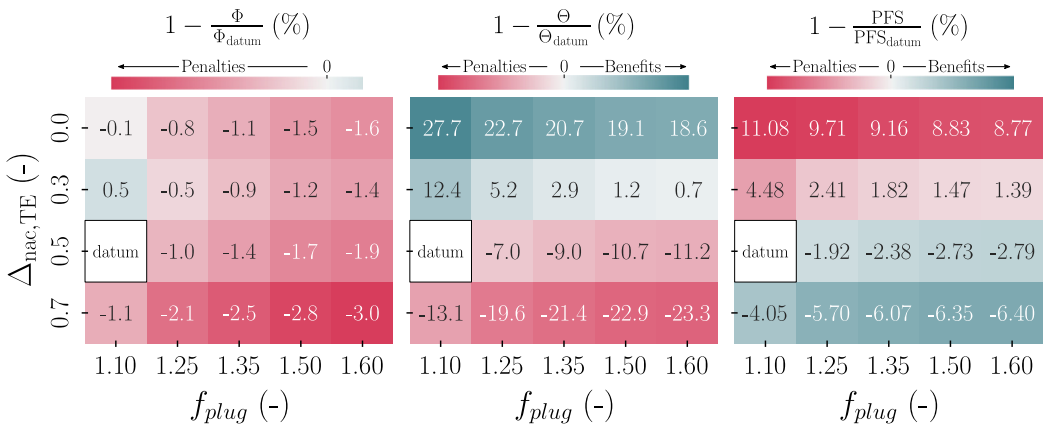


Fig. 12. Computed volumetric rate of viscous dissipation and pressure work, and propulsive force share as a function of droop and plug angles, at datum BLR = 50% and FPR = 1.30, neglecting hade angle effects.

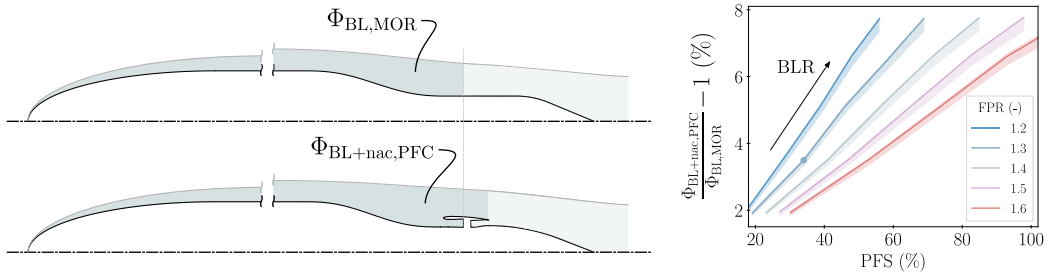


Fig. 13. Integration penalties in terms of viscous dissipation rate between the installed nacelle configuration (PFC) and the baseline morphed fuselage (MOR) with respect to different propulsor sizes, fan operating conditions (colours) and nacelle shapes as explored (shaded areas), with an identified datum (marker) for further comparisons.

5. Flow feature decompositions

It is of interest to segment the flow-field into its different features and breakdown the contributions of Φ and Θ, relative to the overall losses present in the flow Φ_∞ and Θ_∞ (equivalent to the reported Φ and Θ in the previous section, to prevent confusion). As such, the main flow features that are the shear layer, shock and jet plume are analysed, where the latter is further decomposed into the compression, expansion and mixing regions.

5.1. Main and secondary boundary layers

5.1.1. Integration penalties

After isolating the shear layer from the rest of the domain using ξ (Sanders and Laskaridis, 2020), a geometrical split is made at the nacelle's trailing edge whereby its portion upstream is characterised as the BL, and downstream as the wake (Fig. 13). The BL is aimed at being further decomposed into a main BL that forms over the fuselage and the secondary viscous layer that stems from the cowl's leading edge (nac), which both mix above the cowl and combine farther downstream in the wake.

The propulsor integration penalties are first assessed from a BL growth and intrinsic shear losses relative to the morphed fuselage (unintegrated) whose BL is trimmed at the fan-face location of the integrated propulsor (Fig. 13). Despite not being ideal, this geometric split aims at segmenting the BL from the wake in both geometries for a fair comparison where the primary flow entering the fan is then assigned to the jet feature and therefore, its part within the intake should be accounted in the integration losses.

Fig. 13 depicts the shear layers and geometric segmentation for both designs which viscous dissipation rates Φ are given on the right-hand side. Whereas the losses contained within the BL are insensitive to the FPR if plotted versus the BLR, the parameter is included to further decompose the losses when compared with the PFS. A given PFS can be achieved by several BLR and FPR combinations which are given by the different solid lines obtained from the best performing candidates at given BLR and FPR couples yielding different losses, with slight variations given by different nacelle droops, or designs (shades).

5.1.2. Propulsor size influence

In essence, the amount of viscous dissipation within the BL increases with respect to the mass-flow ingested by the fan as the propulsor size increases, yielding a greater wetted surface over the nacelle, which enhances the viscous dissipative effects, insensitively to the FPR. The BL growth caused by the second forming BL favours the shear-stresses in the mixing region of the main and secondary flows over the cowl contributing towards a higher dissipation. Within the propulsor's intake, an extra contribution results from the larger intake length that increases with respect to the amount of mass-flow ingested (as a result of a larger throat area), despite the smaller velocity gradients experienced on the nacelle interior walls. Overall, a minimum increase of 2% in viscous dissipation rate is reported for a fan ingesting 28% of the BL mass-flow. These losses increase up to 8% for the explored design space as the nacelle is scaled up both radially and axially (ingesting the entire BL). This increase in irrecoverable loss is non-negligible as it would need to be mitigated by the jet losses to perform as well as the smaller propulsors.

To further understand how the viscous losses within the BL scale to the overall losses with respect to the propulsor size and fan operating conditions, Fig. 14 depicts the decomposition between the main BL, and the secondary one developing around the propulsor's cowl (nac). All dissipations are non-dimensionalised by the total amount of viscous losses Φ_∞ within the entire domain from the far-field to the Trefftz plane. On the main BL, a decreasing trend indicates that although its

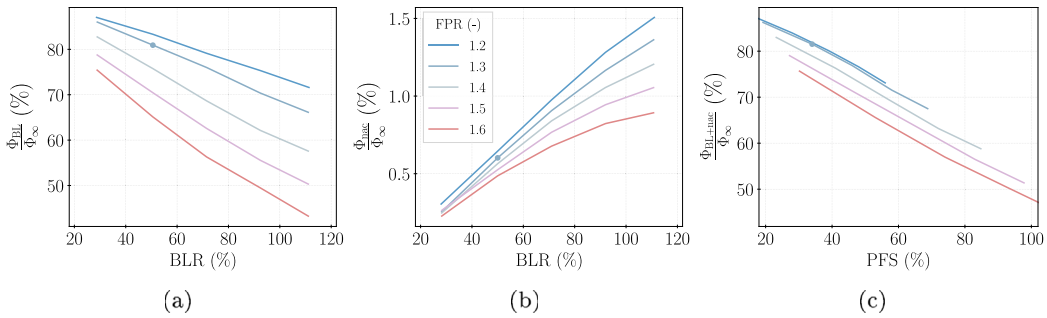


Fig. 14. Computed non-dimensional dissipation in the (a) main, (b) secondary and (c) combined boundary layers for different BLR and FPR combinations, and datum (marker).

absolute contribution increases with the propulsor size, its relative one is outweighed by the larger dissipative effects that take place in the wake and the jet-stream regions as more mass-flow and more pressure is provided to the flow (Fig. 14(a)). Notably, for the design space explored, the relative BL viscous losses vary between 43 and 87% of the overall losses while the absolute BL dissipation amounts to around 89-92.5% of the un-installed baseline drag power which mitigates a maximum recovery of 11% at low BLR.

With the integration of the propulsor, the additional dissipation taking place from the propulsor's cowl is observable in Fig. 14(b) ranging from 0.3 and 1.5% of the total dissipative losses of the design. Nevertheless, this drawback enables energy harvesting before conferring additional power to the flow. Lumping those losses with the former BL, a maximum recovery of 5.5 to 11% is envisaged with these designs when compared against the un-installed baseline.

Lastly, Fig. 14(c) represents the losses contained within the combined BL relative to the overall vehicle's losses. It is noted that for FPR's of 1.2 and 1.3, similar losses portions within the BL are obtained, suggesting that an equivalent remainder is contained within the other features. It is therefore preempted that optima can be found where the jet plume region is the lowest as a larger wake attenuation is achieved, i.e. for a given size greater attenuation results in less wake dissipation as the wake-only feature should remain equivalent.

5.1.3. Nacelle shape influence

Retrieving the results from Fig. 13, changes in the nacelle design for a given size do not largely contribute towards greater losses but scale with respect to the propulsor size. At the particular cluster of BLR = 50% and FPR = 1.30, the nacelle and nozzle shapes influence is evaluated by means of comparison with the best performer (datum). Despite trimming geometrically the BL at the nacelle TE, the plug angle indirectly influences the viscous dissipation by affecting the overall losses present in the domain Φ_∞ by altering its pressure gradients in the surrounding flow, hence its viscous losses portion to the total losses. After ensuring that the hade angles were not influencing the viscous dissipation, Fig. 15 depicts the difference in viscous dissipation rate within the entire BL, i.e. the relative difference between the viscous dissipation rate of a geometry present in the BL and that of the best candidate, labelled as datum.

Relative to datum, negative values represent a higher contribution of the BL losses. It is noted a mere difference between the designs at constant operating conditions with respect to both the nacelle TE inclination and the plug arc and steepness. Notably, the mounted-flush nacelle presents a bell-shaped plug arc favouring the flow acceleration at the exhaust's exit whereas the integrated designed smoothen the plug shape showcasing a strong adverse pressure gradient at the nacelle aft-cowl, decelerating the over-cowl flow velocity and enhancing the shear stress and the viscous dissipation rate. The plug angle has a lower influence on this metric as a larger arc chord merely affects the gradient along the plug arc but presents a larger contribution at the TE of the plug due to the increased steepness.

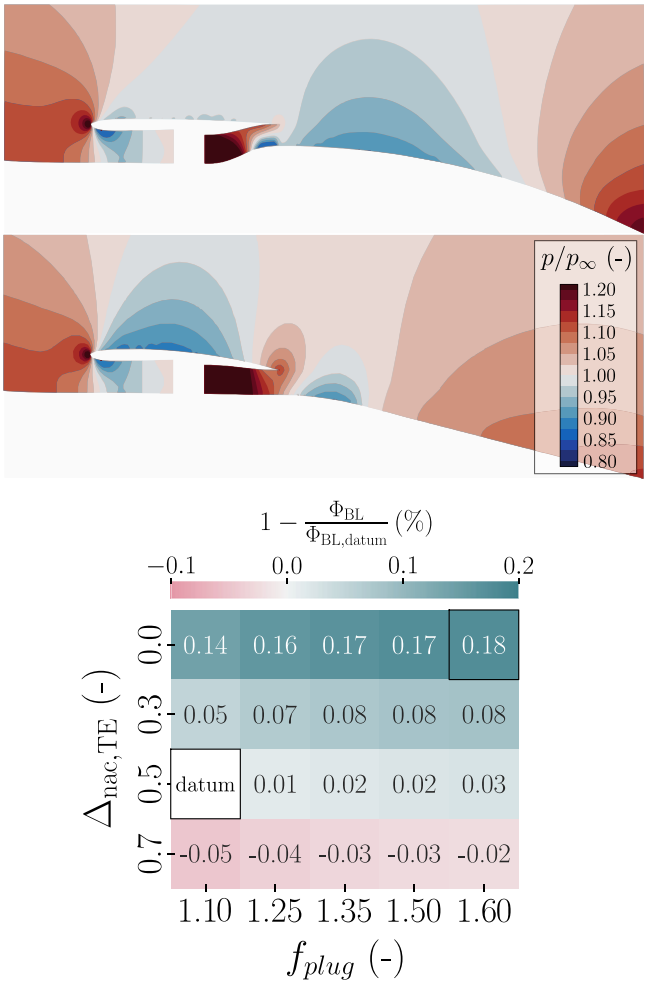


Fig. 15. Normal static pressure contours from the two boxed designs (datum on bottom) with the computed difference in viscous dissipation rate within the BL between datum and the geometries at BLR = 50% and FPR = 1.30.

Overall, it is opined that the geometries experience relatively similar dissipation rates in the BL, with differences below 0.5% (Fig. 13) yielding to between −0.05 and 0.18% relative to the overall propulsive fuselage viscous losses.

Although these integration penalties exist and amount to 2%–8% of additional viscous losses, they are inevitable to allow energy harvesting from the viscous flow. Assuming a through-flow without additional penalties within the propulsor, this leaves larger losses within the wake due to the delay in dissipation which can be mitigated by propelling the fuselage from its aft. To mitigate those losses through the BL ingestion,

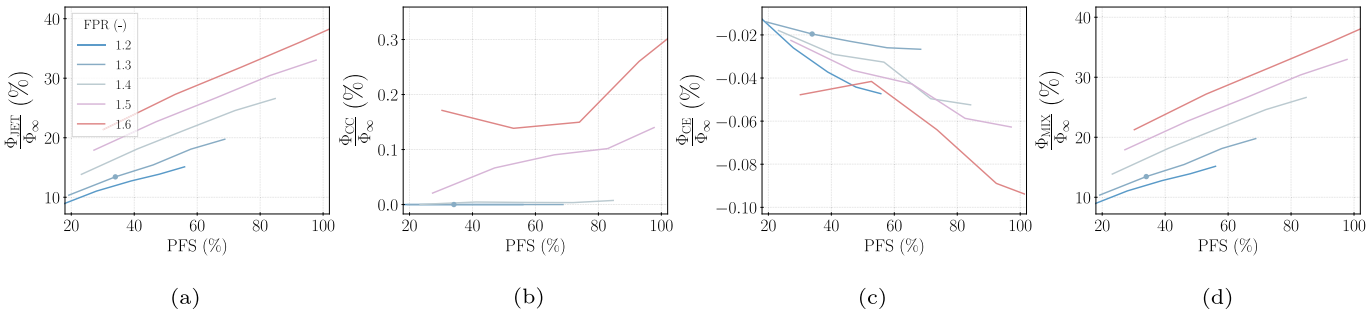


Fig. 16. Computed portion of the viscous dissipation rate in the (a) jet plume, (b) core-compression, (c) core-expansion, and (d) jet/wake mixing regions relative to the overall viscous loss with the previously identified datum design (marker).

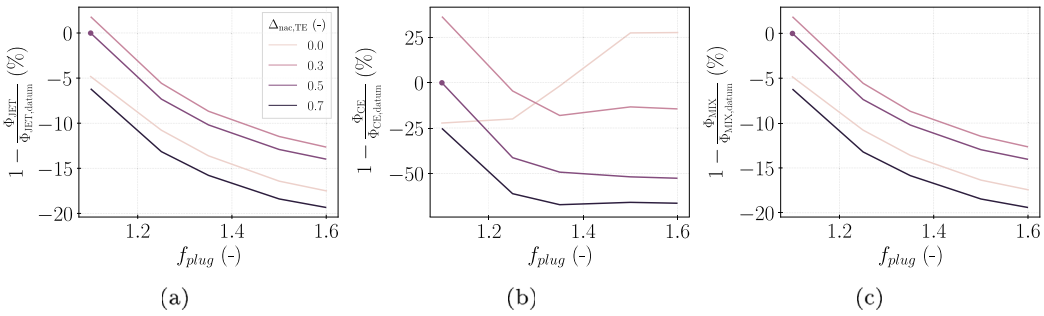


Fig. 17. Computed relative difference in viscous dissipation rate in the (a) jet plume, (b) core-expansion, and (c) jet/wake mixing at BLR = 50% and FPR = 1.30 with datum (marker).

the losses within the jet plume are assessed with respect to the fan operating conditions and propulsor design.

5.2. Propulsive fuselage's plume

5.2.1. Propulsor's operating conditions

A consequence of a larger vehicle surface is a higher drag power contribution that eventually dissipates within the wake. As the amount of mass-flow ingested by the fan grows, a relatively larger dissipation emanates from the larger propulsor's nacelle which directly participates in some integration penalties, as explained. Additionally, the delay in the shear dissipation process implies part of the amount of work imparted into the flow to decay overtime. In comparison with the morphed geometry, the totality of the dissipation that has not happened within the BL, i.e. along the vehicle's surface, would take place behind the aircraft whereas in the case of BLI, an attenuation of that wake is enabled by a partial or total ingestion of the viscous flow.

To initiate the characterisation of this attenuation, the flow leaving the propulsor is identified by the jet-stream identifier Y following the precedence methodology. Fig. 16 respectively depicts the entire jet-stream, and its segmentation into the core-compression and -expansion, and the mixing regions whereby, the power sink Φ is non-dimensionalised by the overall vehicle's viscous dissipation Φ_∞.

Fundamentally, Fig. 16(a) depicts a higher contribution of dissipation within the jet as the mass-flow increases and the mixing losses intensify (Fig. 16(d)). Nonetheless, their rates of progress vary as a coupled effect between BLR and FPR where the amount of additional work provided by the fan is greater than the one harvested. Therefore, it contributes towards larger losses although being responsible for greater propulsive forces. At a target PFS, it appears clear that several propulsor designs meet the requirements but impart a larger loss which is transcribed by a larger power requirement. At larger FPR, shocks are experienced within the jet plume which partly contribute to losses, and intensify with larger mass-flows (Fig. 16(b)). Although their contributions fall below 1% of the overall dissipation, the shocks imply a greater dissipation in their surrounding cells that is not captured from ζ. Numerically, larger losses should be captured in either the core-expansion or mixing regions, as defined per the control volumes, but an unphysical negative loss is reported for the former which is fair to assume that these losses are purely numerical. Although being negative, the values are negligible and the flow is assumed to expand fully isentropically (Fig. 16(c)). The small regions of the flow captured by the core-compression combined with the isentropic nature of the expansion process leave the mixing region, between the wake and the jet, to be the major contribution of losses. These losses increase with both BLR and FPR as more shear stresses are experienced. These stresses result from friction activities between the low velocity of the air particles within the wake that are entrained by the high-speed jet flow. One of the BLI objectives is to mitigate these mixing losses by attenuating the wake from a trade-off between energy harvesting and further energy deposition rate from the fan to fully fill the defects and not contribute towards greater losses, or effectively reduce them.

5.2.2. Exhaust and plug designs influence

The propulsor operating condition is isolated by retrieving the best performing geometry (marked as datum) to solely assess the influence of the droop and plug angles on the losses. The relative difference between all the designs and datum is depicted in Fig. 17 whereby a positive difference suggests a local benefit.

Expectantly, the high radial position of the nacelle TE (mounted-flush) positions the nozzle hub radius also high radially to maintain a choked nozzle with its corresponding surface area. The short arc chord on the plug given by a low f_{plug} accelerates the flow leaving the exhaust potentially leading in separation after a strong shock (at high FPR as observed in Fig. 18). At lower FPR's, a weak shock or series of shocks is observable along the plug's convex surface. The shock forming develops within the jet/wake mixing region which generates strong shear stresses and irrecoverably dissipates the energy into heat.

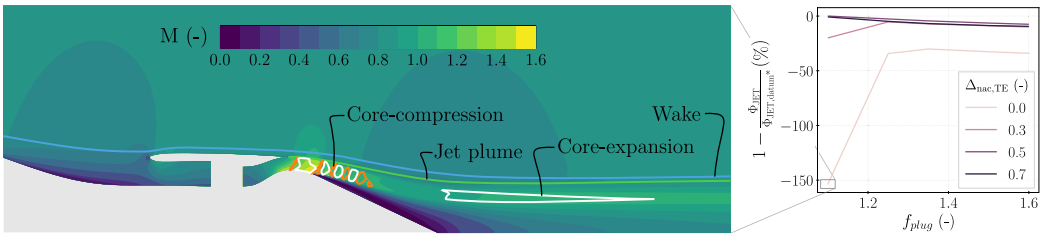


Fig. 18. Mach number contours of the boxed geometry at BLR = 92%, FPR = 1.50, α_{hub} = 0°, f_{plug} = 1.10 and $\Delta_{nac,TE}$ = 0.0, and droop and plug angles effects on the jet viscous dissipation rate.

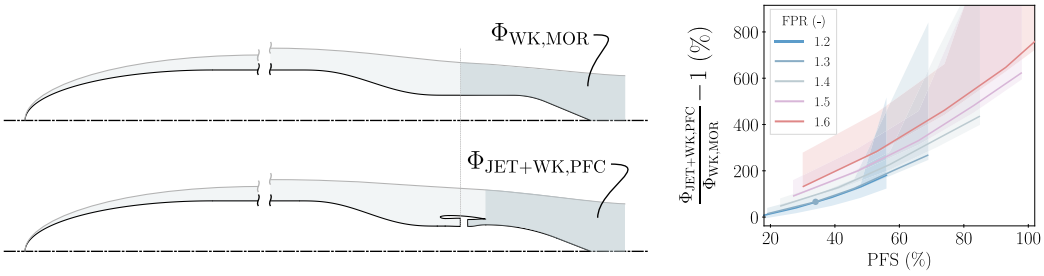


Fig. 19. Viscous dissipation rate attenuation within the jet and wake between the installed nacelle configuration (PFC) and the baseline morphed fuselage (MOR) with respect to different propulsor sizes, fan operating conditions and nacelle shapes as explored (shaded areas), with the previously identified datum design (marker).

Fig. 17(c) depicts a local dissipation increase of 5% in the mixing volume relative to datum whereas the expansion process that follows the shock also experiences part of the dissipation as noted by the −25% difference in Φ_{CE} of Fig. 17(b). Nevertheless, it is reminded that these isentropic losses are a pure product of the numerical split and the large discrepancies with datum are on negligible values. Additionally, the non monotonicity observed for $\Delta_{nac,TE}$ = 0.0 at low plug angles is caused by the rapid flow acceleration generating shocks and separating the flow from the surface. These effects are not noted for the other designs as the nacelle aft is more nested within the fuselage favouring a continuous streamlined flow along the plug.

Apart from this mechanism, a general trend is observed with respect to the plug shape. As the arc chord is extended and the plug cone angle increases downstream, more dissipation occurs within the jet plume (Figs. 17(a) and 18). A stronger adverse pressure gradient (observable in Fig. 15) is experienced by the flow hence showcasing a region of low velocity close to the trailing edge of the vehicle which increases the velocity gradient within the plume and stream recirculation that enhances the shear stresses.

With respect to the offset between the leading and trailing edge radii, the plug angle and its term f_{plug} are also implicitly affected by the changes in the droop. This causes the dissipation phenomena to be partially explained by the above comments made. Notably, a $\Delta_{nac,TE}$ of 0.3 generates less loss than the other designs suggesting that an optimum potentially stands in between 0.0 and 0.5 and therefore a particular exhaust shape combined with a plug arc allows a better utilisation of the energy present in the flow. As the propulsor size increases and ingests more mass-flow, the highly pressurised flow is further accelerated along the bell-shaped plug leaving the wall's surface with a separated region underneath (along the centreline). Intrinsically, these losses are directly related to the arc shape of the plug which causes different degrees of shocks and flow recirculation and mitigation of these losses is enabled by increasing the arc curvature (Fig. 18).

5.3. Wake attenuation

To evaluate the wake attenuation from the different geometries explored, Fig. 19 is used to depict the portion of losses within the jet and wake-only volumes relative to the morphed unintegrated design's wake loss. Similar to the comparison made on the BL with Fig. 13, the best geometries for various propulsor sizes and FPR are given with solid curves where shades represent variations in performance from the different nacelle and plug designs swept.

It is noted that for both FPR of 1.2 and 1.3, similar relative losses are experienced within the jet and wake tending to reduce the wake losses by conveying additional propulsive force. The relative low work input from the fan mitigates the additional losses generated while conveying a mild propulsive force. As the mass-flow increases with wider intakes, more important viscous losses are observed to which variations in designs yield larger undesired differences as shocks and separation are observed along and behind the plug.

The comparison of these jet losses with the amount of work provided by the propulsor, as given in Fig. 20(a) indicates minima in irrecoverable losses in the high-end of BLR where the amount of work provided from the fan to the flow is better used with lower losses to generate a forward force. Nonetheless, a compromise with the contribution of the wake losses needs to be ensured as the jet portion cannot be isolated to assess the performance. In that respect, Fig. 20(b) depicts the contribution of these losses downstream the propulsor relative to the fan power consumption. A distinct change in monotonicity is observed and explained by the conversion of the energy rate into useful work and dissipative losses. For a given amount of mass-flow ingested, increasing the pressure rise across the fan stage contributes towards more forward force but unavoidably to viscous losses which are detrimental to the performance and savings. At a target propulsive force, the optimal size combined with a pressure rise needs to be carefully considered as the nacelle integration effects can outweigh these benefits. In that respect, it is of interest to compare the jet and wake losses relative to the overall losses as well as these overall losses relative to the morphed fuselage (Fig. 21).

Contrasting the losses behind the propulsor with the overall vehicle's losses, Fig. 21(a) highlights the previous findings with almost superimposed performance of the wake attenuation between the two lower ends FPR. Notably, for a target PFS, the larger the FPR the larger the viscous dissipation however, it exists an optimum BLR in which

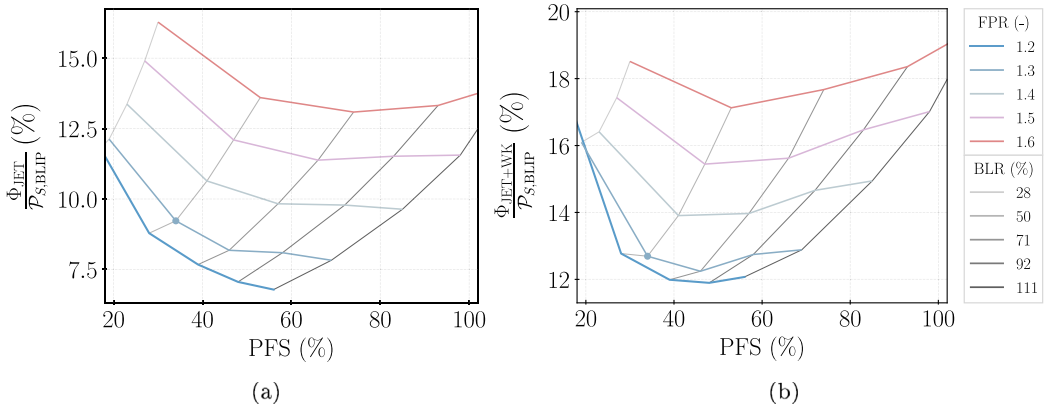


Fig. 20. Computed portion of viscous dissipation rate in (a) the jet and (b) the jet and wake, relative to the power demand from the aft-mounted fan to provide the pressure rise targeted.

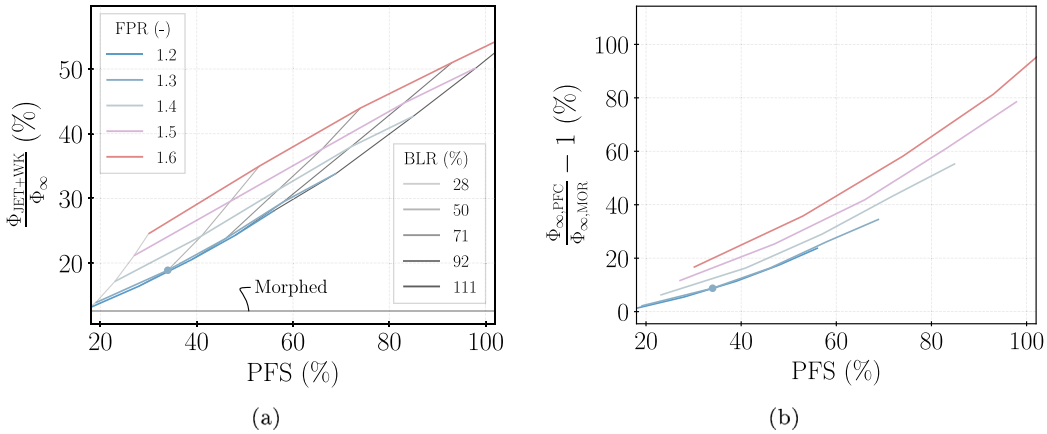


Fig. 21. Computed (a) portion of viscous dissipation rate in the jet and wake relative to the wake of the baseline morphed fuselage (MOR) with respect to different propulsor sizes, fan operating conditions and (b) total viscous losses between the powered and unpowered fuselages.

those losses are mitigated by utilising better the energy rate imparted by the fuselage.

The combination of the two previously described relations yield Fig. 21(b) giving the relative amount of total viscous losses between the unpowered and powered fuselages. It can be observed additional losses of 10% for relatively small propulsor geometries ingesting up to 70% of the BL mass-flow and providing up to 40% of the forward force requirement from the aircraft.

6. Conclusion

The intricate interactions inherent to highly coupled engine–airframe aerodynamics present an opportunity to employ energy-based methodologies for a deeper and more physically intuitive understanding of aero-propulsive systems. While alternative bookkeeping schemes based on momentum and control volume analyses exist, these primarily rely on pressure and skin-friction decompositions, which can limit the depth of insight provided. This study leverages an energy-based framework, formulated within an absolute reference frame, to investigate the work–energy relationships governing flight. By modelling the aircraft as displacing initially quiescent air, the approach captures energy deposition and viscous layer formation — mechanisms that can be harnessed by an integrated propulsor to yield fuel savings in turbo-electric thrust-splitting configurations.

Beyond the primary effects governed by the boundary layer ratio (BLR) and fan pressure ratio (FPR), the exploration of rear-end design space for a propulsive fuselage concept identifies the critical variables influencing aero-propulsive performance. A precedence-based methodology is introduced to decompose the flow field into causal features, enabling a clearer understanding of energy deposition, transfer, and loss. This method quantifies the contributions of pressure work and viscous dissipation rates to the total energy loss experienced by the aircraft. Although the majority of energy within the viscous layer is irreversibly dissipated prior to reaching the aft-mounted fan, recoveries of 6%–11% of the available energy are demonstrated.

To assess integration penalties and wake attenuation effects, a morphed baseline configuration is compared against its integrated counterpart. The flow field is segmented into primary features, revealing losses originating from the wake induced by spilled-over cowl flow. These losses are mitigated through interaction with the jet plume, whose attenuation and dissipation behaviour is further characterised. This investigation of aft-body designs leads to the following key findings:

- Propulsor size and fan pressure ratio are the dominant drivers of aero-propulsive performance, with optimal combinations balancing power demand for a given force share;
- Nacelle trailing edge droop dictates the direction of the core flow exiting the propulsor, significantly affecting work application and loss — embedded nacelle designs are shown to offer performance benefits;
- Nozzle and plug curvature contribute to loss reduction by preventing early detachment along surface walls;
- Steep plug angles induce recirculation behind the aircraft, whereas slender nozzles are shown to enhance performance, particularly for the smaller propulsors considered in this study.

Design space analysis reveals that maximum savings are achieved when the propulsive fuselage ingests approximately 50% of the fuselage boundary layer mass flow. When retrofitted with two under-wing turbofans at their original scale, operating at off-design, a fuel saving coefficient of 10.5% is attained, contributing roughly one-third of the total thrust. These estimates remain optimistic due to the absence of three-dimensional geometrical effects. More realistic assessments will require future work focused on re-scaling the primary powerplants for reduced thrust, employing propulsors with elongated plug-cones to prevent flow separation, and optimising the aft-mounted fan design while incorporating 3D effects. Further development of the corrected kinetic energy inflow rate term ($\mathcal{P}_K^*$), in conjunction with improved fidelity of propulsion models, is expected to support more accurate prediction of propulsive power and facilitate analytical evaluation of irrecoverable losses within the propulsion domain.

This study demonstrates the utility of energy-based methods, combined with flow feature segmentation, in supporting the design of boundary layer ingestion aircraft. By providing a physically grounded framework for understanding energy deposition, transfer, and dissipation, this approach offers valuable insights into the aerodynamic interactions that govern the performance of highly integrated propulsion–airframe configurations, including hybrid-wing and lifting fuselage concepts.

CRediT authorship contribution statement

Nicolas G.M. Moirou: Writing – review & editing, Writing – original draft, Visualization, Validation, Methodology, Investigation, Data curation, Conceptualization. **Drewan S. Sanders:** Writing – review & editing, Supervision, Project administration.

Declaration of competing interest

The authors declare that they have no known competing financial interests or personal relationships that could have appeared to influence the work reported in this paper.

Acknowledgements

This work was conducted within the SUBLIME (Supporting Understanding of Boundary-Layer Ingestion Model Experiment) project as part of the Clean Sky 2 Joint Undertaking which has received funding from the European Union's Horizon 2020 research and innovation program under Grant Agreement No. 864803.

Data availability

Data will be made available on request.

References

ANSYS, Inc., 2020a. Ansys® fluent release 20.2.

ANSYS, Inc., 2020b. Ansys® ICEM CFD release 20.2.

Arntz, A., Atinault, O., Merlen, A., 2015. Exergy-based formulation for aircraft aeropropulsive performance assessment: Theoretical development. AIAA J. 53 (6), 1627–1639. http://dx.doi.org/10.2514/1.J053467.

Arntz, A., Hue, D., 2016. Exergy-based performance assessment of the NASA common research model. AIAA J. 54 (1), 88–100. http://dx.doi.org/10.2514/1.J054127.

Battiston, A., Ponza, R., Benini, E., 2021. Design exploration for an axisymmetric rear BLI propulsor. In: AIAA Propulsion and Energy Forum. American Institute of Aeronautics and Astronautics, Virtual Event, http://dx.doi.org/10.2514/6.2021-3470.

Drela, M., 2009. Power balance in aerodynamic flows. AIAA J. 47 (7), 1761–1771. http://dx.doi.org/10.2514/1.42409.

Drela, M., 2021. Considerations in aerodynamic force decomposition. In: AIAA Aviation 2021 Forum. American Institute of Aeronautics and Astronautics, Virtual Event, http://dx.doi.org/10.2514/6.2021-2552.

Epstein, A.H., 2013. Aeropropulsion for commercial aviation in the twenty-first century and research directions needed. AIAA J. 52 (5), 901–911. http://dx.doi.org/10.2514/1.J052713.

European Commission, 2011. Flightpath 2050 Europe's vision for aviation. http://dx.doi.org/10.2777/50266.

Gray, J.S., Mader, C.A., Kenway, G.K., Martins, J.R.R.A., 2018. Modeling boundary layer ingestion using a coupled aeropropulsive analysis. J. Aircr. 55 (3), 1191–1199. http://dx.doi.org/10.2514/1.C034601.

Gray, J.S., Mader, C.A., Kenway, G.K.W., Martins, J.R.R.A., 2020. Coupled aeropropulsive optimization of a three-dimensional boundary-layer ingestion propulsor considering inlet distortion. J. Aircr. 57 (6), 1014–1025. http://dx.doi.org/10.2514/1.C035845.

Habermann, A.L., Gokhale, A., Hornung, M., 2021. Numerical investigation of the effects of fuselage upsweep in a propulsive fuselage concept. CEAS Aeronaut. J. 12, 173–189. http://dx.doi.org/10.1007/s13272-020-00487-2.

Lovely, D., Haimes, R., 1999. Shock detection from computational fluid dynamics results. In: 14th Computational Fluid Dynamics Conference. AIAA, pp. 296–304. http://dx.doi.org/10.2514/6.1999-3285.

Matesanz-García, J., Piovesan, T., MacManus, D.G., 2022. Aerodynamic optimization of the exhaust system of an aft-mounted boundary layer ingestion propulsor. Internat. J. Numer. Methods Heat Fluid Flow 33, 1295–1318. http://dx.doi.org/10.1108/HFF-06-2022-0362.

MIDAP Study Group, 1979. Guide to In-Flight Thrust Measurement of Turbojets and Fan Engines. Tech. Rep. AGARD-AG-237, p. 212.

Moirou, N.G.M., 2023. Aero-propulsive Performance Assessment Approach to Boundary Layer Ingestion Aircraft (Ph.D. thesis). Cranfield University, Cranfield, United Kingdom.

Moirou, N.G.M., Mutangara, N.E., Sanders, D.S., 2024. Fundamental considerations in the design and performance assessment of propulsive fuselage aircraft concepts. Aeronaut. J. 129, http://dx.doi.org/10.1017/aer.2024.124.

Moirou, N.G.M., Sanders, D.S., 2025. Performance evaluation approach for design space explorations of propulsive fuselage aircraft concepts. CEAS Aeronaut. J. 16, http://dx.doi.org/10.1007/s13272-025-00830-5.

Moirou, N.G.M., Sanders, D.S., Laskaridis, P., 2023. Advancements and prospects of boundary layer ingestion propulsion concepts. Prog. Aerosp. Sci. 138, 100897. http://dx.doi.org/10.1016/J.PAEROSCI.2023.100897.

Sanders, D.S., 2018. Boundary Layer Ingestion Performance Assessments with Application to Business Jets (Ph.D. thesis). Cranfield University, Cranfield, United Kingdom.

Sanders, D., 2023. Aircraft Aerodynamic Work-Energy Relationships with Mass Source Considerations. Tech. Rep. RP002, Cranfield University, Cranfield, United Kingdom.

Sanders, D.S., Laskaridis, P., 2020. Full-aircraft energy-based force decomposition applied to boundary-layer ingestion. AIAA J. 58 (10), 4357–4373. http://dx.doi.org/10.2514/1.J058695.

Sato, S., 2012. The Power Balance Method For Aerodynamic Performance Assessment (Ph.D. thesis). Massachusetts Institute of Technology, Massachusetts, USA.

Seitz, A., Peter, F., Bijewitz, J., Habermann, A.L., 2018. Concept validation study for fuselage wake-filling propulsion integration. In: 31st Congress of International Council of the Aeronautical Sciences. Belo Horizonte, Brazil.

Tse, T.S., 2021. Aerodynamics and Power Balance of Boundary Layer Ingesting Aircraft (Ph.D. thesis). (September), University of Cambridge, Cambridge, UK.

Walsh, P.P., Fletcher, P., 2004. Gas Turbine Performance, second ed. Blackwell Science, p. 664.

Welstead, J.R., Felder, J.L., 2016. Conceptual design of a single-aisle turboelectric commercial transport with fuselage boundary layer ingestion. In: 54th AIAA Aerospace Sciences Meeting. http://dx.doi.org/10.2514/6.2016-1027.

Wislicenus, G.F., 1960. Hydrodynamics and propulsion of submerged bodies. Am. Rocket. Soc. J. 30 (12), 1140–1148. http://dx.doi.org/10.2514/8.5351.

Yildirim, A., Gray, J.S., Mader, C.A., Martins, J.R.R.A., 2022. Boundary-layer ingestion benefit for the STARC-ABL concept. J. Aircr. 59 (4), 896–911. http://dx.doi.org/10.2514/1.C036103.

Zhao, X., Yao, H., 2022. BLI Turbofan Performance Maps. Tech. Rep. RP0019, Chalmers University of Technology, Gothenburg, Sweden.



https://dspace.org/

Work-energy pathway analysis of boundary layer ingestion in propulsive fuselage aircraft

Moirou, Nicolas G. M.; Sanders, Drewan S.

2026-06
Elsevier
https://doi.org/10.1016/j.ijheatfluidflow.2026.110336
Moirou NGM, Sanders DS. (2026) Work-energy pathway analysis of boundary layer ingestion in propulsive fuselage aircraft. International Journal of Heat and Fluid Flow, Volume 120, June 2026, Article number 110336

Downloaded from a DSpace repository. https://dspace.org/